

Complex Antiferromagnetic Order in the Metallic Triangular Lattice Compound $\text{SmAuAl}_4\text{Ge}_2$

Keke Feng,^{*} Caleb Bush,[†] Olatunde Oladehin,^{*} Minhyea Lee,[‡] and Ryan Baumbach^{*}
(Dated: January 3, 2024)

The compounds $\text{LnAuAl}_4\text{Ge}_2$ ($\text{Ln} = \text{lanthanide}$) form in a structure that features two-dimensional triangular lattices of Ln ions that are stacked along the crystalline c axis. Together with crystal electric field effects, magnetic anisotropy, and electron-mediated spin exchange interactions, this sets the stage for the emergence of strongly correlated spin and electron phenomena. Here we investigate $\text{SmAuAl}_4\text{Ge}_2$, which exhibits weak paramagnetism that strongly deviates from conventional Curie-Weiss behavior. Complex antiferromagnetic ordering emerges at $T_{\text{N}1} = 13.2$ K and $T_{\text{N}2} = 7.4$ K, where heat capacity measurements show that these transitions are first and second order, respectively. These measurements also reveal that the Sommerfeld coefficient is not enhanced compared to the nonmagnetic analog $\text{YAuAl}_4\text{Ge}_2$, consistent with the charge carrier quasiparticles exhibiting typical Fermi liquid behavior. The temperature-dependent electrical resistivity follows standard metallic behavior, but linear magnetoresistance unexpectedly appears within the ordered state. We compare these results to other $\text{LnAuAl}_4\text{Ge}_2$ materials, which have already been established as localized f -electron magnets that are hosts for interesting magnetic and electronic phases. From this, $\text{SmAuAl}_4\text{Ge}_2$ emerges as a complex quantum spin metal, inviting further investigations into its properties and the broader family of related materials.

PACS numbers: PACS

I. INTRODUCTION

Geometrically frustrated magnetic materials historically have attracted substantial interest as reservoirs for novel quantum phases [1–4]. A prototypical example is the insulating two-dimensional triangular antiferromagnetic spin lattice, where early theoretical efforts indicated that the ground state for spin $S = 1/2$ does not exhibit long-range order [5]. Later numerical studies modified this model by showing that 120° order can emerge when antiferromagnetic nearest neighbor spin interactions are included [6–9]. Since then, substantial experimental studies have been carried out for insulators with triangular nets of transition metal elements, many of which exhibit complex magnetic phenomena [10–13]. Efforts have also been extended to lanthanide-containing systems, where the f -electron wave function is well localized by comparison to d -electron analogs. This results in weakened exchange couplings and large g -factors, producing rich phase diagrams with easily tuned ground states: e.g., using magnetic fields [14, 15]. More recently, related semimetal and metal systems have also been studied, where the presence of conduction electrons leads to long-range magnetic exchange interactions that are mediated by the Ruderman-Kittel-Kasuya-Yosida (RKKY) mechanism [16–18]. In addition to enhancing the degrees of freedom, this enables opportunities to explore the emergence of flat bands [19, 20], exotic superconductivity [21, 22], skyrmion phases [23], unconventional Hall

effects [24, 25], and potentially even metallic quantum spin liquids [26].

This motivated us to examine the compounds $\text{LnTAl}_4\text{Ge}_2$ ($\text{Ln} = \text{lanthanide}$ and $T = \text{transition metal}$), which feature triangular nets of Ln ions [27] (Fig. 1). Studies of the $\text{Ln} = \text{Ce, Nd, Gd, and Tb}$ variants have recently revealed complex ordering, indications of magnetic frustration, and complex temperature-magnetic field ($T-H$) phase diagrams. For example, $\text{CeAuAl}_4\text{Ge}_2$ hosts trivalent cerium moments with evidence for a ferromagnetic interaction within the triangular ab -plane, which might relieve spin frustration [28]. In the case of $\text{NdAuAl}_4\text{Ge}_2$, the spins prefer to orient along the c -axis, two magnetic phase transitions are observed ($T_{\text{N}1} = 1.75$ K and $T_{\text{N}2} = 0.49$ K), and several metamagnetic phase transitions are seen for magnetic fields applied along the c -axis [31]. Even more complex behavior is seen for $\text{GdAuAl}_4\text{Ge}_2$ and $\text{TbAuAl}_4\text{Ge}_2$, which exhibit multiple transitions at substantially higher ordering temperatures, easy- ab -plane anisotropy, and multiple anisotropic metamagnetic phase transitions for magnetic fields applied in the triangular net plane [29, 30]. Finally, it is noteworthy that $\text{CePtAl}_4\text{Ge}_2$ exhibits heavy fermion antiferromagnetism, showing that Kondo lattice physics impacts behavior in some cases [32]. Thus, it is natural to anticipate that further variation of the Ln ion could produce other novel phenomena resulting from the combination of crystal electric field effects, complex RKKY interactions, geometric frustration, and strong electronic correlations.

Here we focus on $\text{SmAuAl}_4\text{Ge}_2$, where the f -electron state is likely to be distinct from that of its lanthanide neighbors. In particular, samarium f -electrons can (i) adopt either a divalent ($4f^6$; $J = 0$) or trivalent ($4f^5$; $J = 5/2$) configuration, with crystal electric field splitting, (ii) hybridize with conduction electron states, and

^{*} Department of Physics, Florida State University.; National High Magnetic Field Laboratory

[†] Department of Physics, Rochester Institute of Technology.

[‡] Department of Physics, University of Colorado, Boulder.; National High Magnetic Field Laboratory

(iii) exhibit van Vleck paramagnetism due to the ground state ($J = 5/2$) and first excited state ($J = 7/2$) being separated by a relatively small energy [33, 34]. This generates interesting behavior in other model systems, including (i) heavy fermion ground states in $\text{SmOs}_4\text{Sb}_{12}$ [35, 36], $\text{SmPt}_4\text{Ge}_{12}$ [37], and $\text{SmTi}_2\text{Al}_{20}$ [38]; (ii) topological Kondo insulating behavior in SmB_6 [39, 40]; (iii) coexistence of superconductivity and magnetism in SmRh_4B_4 [41]; and (iv) valence instabilities in samarium monochalcogenides [42].

From magnetization, heat capacity, and electrical transport measurements, we show that $\text{SmAuAl}_4\text{Ge}_2$ exhibits strong deviations from conventional Curie-Weiss paramagnetism at elevated temperatures due to crystal electric field splitting of the $J = 5/2$ multiplet, and possibly other effects. Complex antiferromagnetic ordering appears at $T_{N1} = 13.2$ K and $T_{N2} = 7.4$ K, which are first and second order transitions, respectively. Metallic behavior without evidence for enhanced mass charge carrier quasiparticles is seen in the electronic coefficient of the heat capacity and electrical transport measurements, resembling what is seen for the nonmagnetic analog $\text{YAuAl}_4\text{Ge}_2$. Interestingly, although applied magnetic fields up to 9 T have little effect on the ordering temperatures, linear magnetoresistance resembling what is seen for $\text{GdAuAl}_4\text{Ge}_2$ and $\text{TbAuAl}_4\text{Ge}_2$ [29, 30] is observed within the ordered state. Thus, $\text{SmAuAl}_4\text{Ge}_2$ emerges as an intriguing addition to the $\text{LnAuAl}_4\text{Ge}_2$ family, where complex magnetic ordering and unusual magnetotransport behavior are observed within an ensemble of f -electron spins whose high-temperature paramagnetism differs significantly from other Ln analogs.

II. EXPERIMENTAL METHODS

$\text{SmAuAl}_4\text{Ge}_2$ single crystals were grown using an aluminum molten metal flux following the procedure detailed in Refs. [27, 28]. In order to allow comparison to a non- f -electron containing analogue, single crystal specimens of $\text{YAuAl}_4\text{Ge}_2$ were produced using the same method. Crystals typically form as three-dimensional clusters, where individual crystals with dimensions on the order of 2 mm and hexagonal or triangular facets associated with the ab plane can be isolated (Fig. 1). Room temperature powder x-ray diffraction (PXRD) measurements were performed using a Rigaku SmartLab SE X-ray diffractometer with a $\text{Cu K}\alpha$ source. The Rietveld refinement analysis was done using GSAS-II to assess the purity and determine the structure parameters. The principal c -axis was identified by measuring the diffraction pattern on polished flat crystals using the same system and was also apparent in the crystal shape.

Temperature (T) dependent magnetization M measurements were carried out for $T = 1.8 - 300$ K under magnetic fields of $\mu_0 H = 0.5$ T applied parallel (\parallel) and perpendicular (\perp) to the crystallographic c -axis using a Quantum Design VSM Magnetic Property Measurement

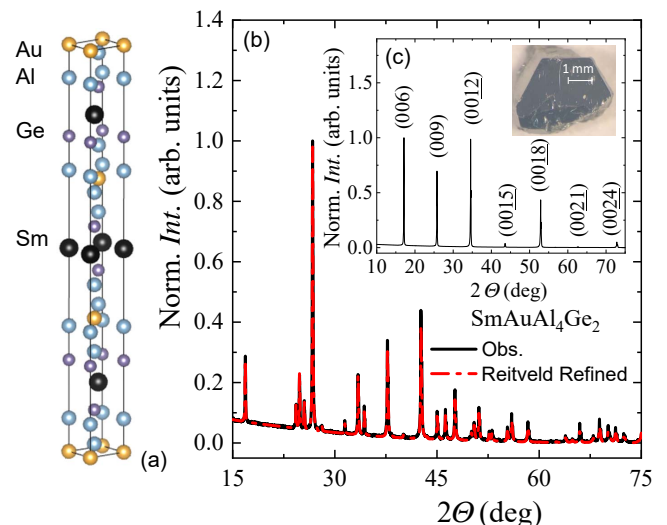


FIG. 1. (a) Crystal structure of $\text{SmAuAl}_4\text{Ge}_2$ [43]. (b) Rietveld refinement of the powder X-ray diffraction pattern for $\text{SmAuAl}_4\text{Ge}_2$. The black line is the observed experimental pattern, and the red dashed line is the calculated pattern. Inset: A single crystal specimen obtained from the aluminum flux growth method described in the text. (c) XRD patterns of a c -axis aligned $\text{SmAuAl}_4\text{Ge}_2$ single crystal similar to that shown in the inset.

System. Data were collected (i) under zero field cooled (ZFC) conditions, where the sample was cooled to $T = 1.8$ K, the magnetic field was applied, and M was measured as T increased to 300 K and (ii) field cooled (FC) conditions, where the magnetic field was applied at 300 K and M was measured as T decreased to 1.8 K. Isothermal magnetization measurements were also performed for $\mu_0 H \leq 7$ T, where the sample was zero field cooled prior to the measurement at each temperature. Heat capacity C measurements were performed for $T = 1.8 - 40$ K in a Quantum Design Physical Properties Measurement System using a conventional thermal relaxation technique. Electrical resistivity ρ measurements for $T = 1.8 - 300$ K and magnetic fields $\mu_0 H \leq 9$ T were performed in a four-wire configuration for polished single crystal using the same system. For $\rho(T)$, both ZFC and FC measurements were performed. For $\rho(H)$, samples were zero field cooled prior to measurements.

III. RESULTS

The trigonal $\text{SmAuAl}_4\text{Ge}_2$ unit cell is shown in Fig. 1(a). The powder X-ray diffraction pattern for $\text{SmAuAl}_4\text{Ge}_2$ is shown in Fig. 1(b), where the data are described by the trigonal $\text{LnAuAl}_4\text{Ge}_2$ structure (space group $R\bar{3}m$ (No. 166) [27]). A Rietveld refinement yields lattice parameters and a unit cell volume $a = 4.21711(10)$ Å, $31.1452(6)$ Å, and $V = 479.680(13)$, consistent with expectations for the trivalent lanthanide contraction for

Site Label	x, y, z	occupancy	U_{iso}
Al2	0, 0, 0.08089	1	0.0199
Ge	0, 0, 0.22380	1	0.0136
Al1	0, 0, 0.31009	1	0.0538
Sm	0, 0, 0.50000	1	0.0027
Au	0, 0, 0	1	0.0018

TABLE I. Summary of crystallographic parameters resulting from Rietveld refinement of the data using GSAS-II. Fits yielded the lattice constants $a = 4.21711(10)$ Å, $31.1452(6)$ Å, and $V = 479.680(13)$. The quality of the fit is characterized by $R_W = 7.76$.

$LnAuAl_4Ge_2$ discussed in Ref. [29]. Other fit parameters are summarized in Table I. Fig. 1(c) shows the XRD pattern for a c -axis aligned crystal of $SmAuAl_4Ge_2$, exhibiting only the $(00l)$ diffraction peaks. This reveals that the naturally occurring hexagonal facets are aligned in the ab plane.

The temperature-dependent magnetic susceptibilities for magnetic fields $\mu_0 H$ applied parallel ($\chi_{\parallel}(T)$) and perpendicular ($\chi_{\perp}(T)$) to the crystallographic c -axis for $SmAuAl_4Ge_2$ are shown in Fig. 2. Weak easy ab -plane anisotropy is observed in the paramagnetic state, where: (i) $\chi_{\parallel}(T)$ initially decreases with decreasing T , evolves through a broad minimum centered near 175 K, and exhibits a gradual increase down to 20 K and (ii) $\chi_{\perp}(T)$ weakly decreases below 300 K, goes through a broad minimum near 250 K, and exhibits a broad maximum centered around 50 K. This behavior is distinct from what is seen for other lanthanides with localized f -states, but resembles results for some samarium containing intermetallics and points towards the samarium ions having a trivalent f -electron configuration where the $J = 5/2$ multiplet is strongly impacted by crystal electric field splitting below 300 K.

Antiferromagnetic phase transitions emerge near $T_{N1} = 13.2$ K and $T_{N2} = 7.4$ K. The details of this behavior are shown in Figs. 2(b) and 2(c), where $\chi_{\parallel}(T)$ is strongly reduced following each transition and weak hysteresis is observed around T_{N2} . The origin of the hysteresis is not obvious, but we speculate that it indicates the formation of history-dependent magnetic domains within the ordered state. In contrast, $\chi_{\perp}(T)$ weakly increases and then decreases at T_{N1} and T_{N2} , respectively. These trends reveal that the magnetic ordering is characterized by progressively strengthening anti-alignment of the spins along the c -axis, with a weak co-alignment of spins at T_{N1} and a weak anti-alignment at T_{N2} for the in-plane configuration. The occurrence of multiple phase transitions resembles what is seen for $LnAuAl_4Ge_2$ analogs that exhibit conventional Curie-Weiss magnetism [29, 30], indicates the presence of competing magnetic exchange interactions, and further clarifies how the magnetic anisotropy varies with Ln . To further investigate the ordered state, isothermal magnetization measurements were performed at $T = 1.8$ K. As seen in Fig. 2(d), $M(H)$ increases linearly with $\mu_0 H \leq 7$ T, with no evidence for metamagnetic

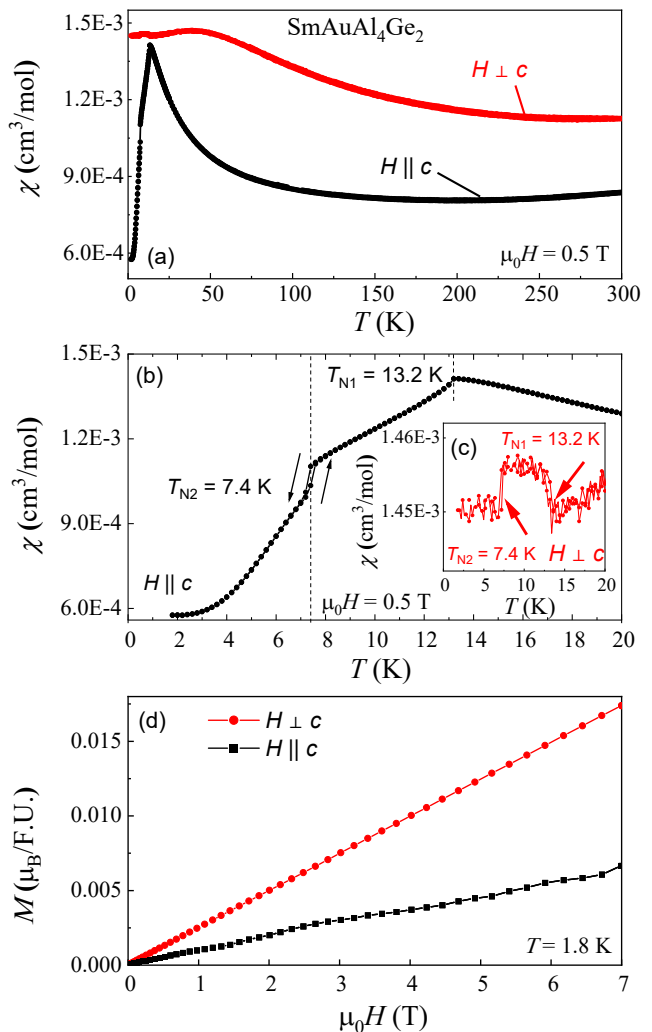


FIG. 2. (a) Temperature dependent magnetic susceptibility $\chi(T)$ for $SmAuAl_4Ge_2$ for magnetic fields $\mu_0 H = 0.5$ T applied parallel (\parallel) and perpendicular (\perp) to the c axis. Data were collected both for zero field cooling and field cooling, as described in the experimental methods. (b,c) Zoom of $\chi(T)$ at low temperatures for magnetic fields $\mu_0 H = 0.5$ T applied (b) parallel (\parallel) and (c) perpendicular (\perp) to the c axis, emphasizing the magnetic phase transitions. The dotted vertical lines in (b) represent the locations of the ordering temperatures T_{N1} and T_{N2} . (d) Isothermal magnetization $M(H)$ for both field directions at $T = 1.8$ K.

phase transitions for both field directions. This contrasts with what is seen for the $Ln = Nd, Gd,$ and Tb analogs, which all show a rich variety of anisotropic metamagnetic phase transitions. Evidence for quantum oscillations is also seen for $H \parallel c$, indicating the high quality of these crystals.

The heat capacity divided by temperature C/T data for $SmAuAl_4Ge_2$ are compared to that of the $J = 0$ nonmagnetic analog $YAuAl_4Ge_2$ in Fig. 3. As expected, there are qualitative similarities between these curves at elevated temperatures where phonons dominate C/T , al-

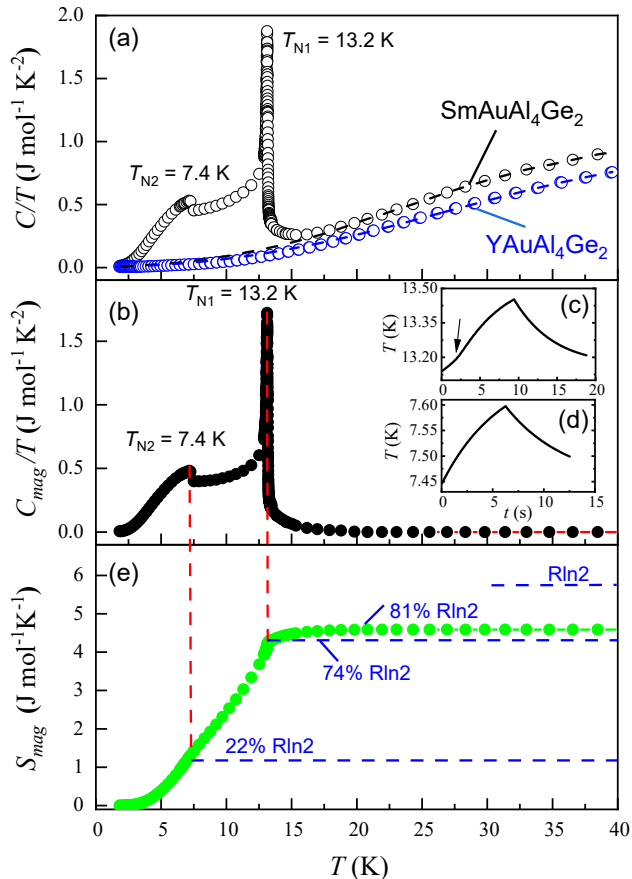


FIG. 3. (a) The heat capacity divided by temperature C/T vs. T for single-crystal $\text{SmAuAl}_4\text{Ge}_2$ and $\text{YAuAl}_4\text{Ge}_2$ at $T = 1.8 - 40 \text{ K}$. The dotted lines represent the fits that are described in the text. (b) The magnetic heat capacity divided by temperature C_{mag}/T vs. T plotted for $\text{SmAuAl}_4\text{Ge}_2$. (c,d) The relaxation curves around T_{N1} (c) and T_{N2} (d). In panel (c), the arrow indicates the kink in the heating curve due to the latent heat of the first-order phase transition. A similar feature is not detected around T_{N2} . (e) Magnetic entropy S_{mag} vs. T , which is obtained from the heat capacity data as described in the text.

though the Sm curve lags behind the Y curve with decreasing temperature. Similar behavior is observed in other lanthanide series when the mass of the non- $4f$ ion differs from that of the $4f$ ion [44]. To account for this difference, fits to the data (dashed lines) were done using the expression,

$$C(T) = \gamma T + C_{\text{Debye}} \quad (1)$$

where γ is the electronic coefficient of the heat capacity and C_{Debye} is the Debye integral function. These fits yield $\gamma \approx 5 \text{ mJ mol}^{-1} \text{K}^{-2}$ for both compounds and Debye temperatures $\theta_D = 242 \text{ K}$ and 220 K for $\text{YAuAl}_4\text{Ge}_2$ and $\text{SmAuAl}_4\text{Ge}_2$, respectively. These γ values resemble what was seen for the Gd and Tb analogues [29, 30], indicating that the electronic band states are similar, and

the primary factors that lead to differences in the heat capacities are the distinct f -electron states that are seen for different lanthanides.

There are two pronounced peaks in $C(T)$ at T_{N1} and T_{N2} . The feature at T_{N1} is sharp and abrupt, and an examination of the heat pulse relaxation curve $T(t)$ reveals evidence for there being a latent heat, as expected for a first-order phase transition (Fig. 3(c)). To account for this, in the vicinity of T_{N1} , the data were analyzed using a single slope expression[45], resulting in the curve shown in Fig. 3. For the peak near T_{N2} , the relaxation curves indicate that it is second order (Fig. 3(d)). To determine the magnetic contribution to the entropy $S_{\text{mag}}(T)$ (Fig. 3(e)), we isolate the magnetic contribution to the heat capacity ($C_{\text{mag}}/T = C_{\text{Sm}}/T - (\gamma T + C_D/T)$) and then integrate it ($S_{\text{mag}}(T) = \int_0^T C_{\text{mag}}/T dT$). $S_{\text{mag}}(T)$ reaches $4.28 \text{ J mol}^{-1} \text{K}^{-1}$ at T_{N1} , which is 74% of the value expected for a doublet ground state ($R \ln 2$) and is strongly reduced from the full $J = 5/2$ value ($R \ln 6$). This is consistent with the perspective from $\chi(T)$ measurements that crystal electric field splitting impacts the low temperature f -state behavior. However, we also note that despite the good agreement between C/T and the Debye fit, the finding that $S_{\text{mag}} < R \ln 2$ may imply that phonon background subtraction is an overestimate. As described below, crystal electric field splitting plays an important role over this temperature range, which is not considered in this analysis of the data.

Figs. 4(a)-4(c) shows the temperature-dependent electrical resistivity $\rho(T)$ with the electrical current I applied in the ab plane and magnetic fields applied either in the ab plane or along the c axis. Consistent with the metallic behavior that is observed for other lanthanide variants [29, 30], the room temperature resistivity is near $20 \mu\Omega \text{ cm}$ and decreases with decreasing T . At low temperatures, the magnetic ordering is preceded by a weak minimum that is centered near 20 K . Similar behavior was seen for $\text{GdAuAl}_4\text{Ge}_2$ [29], where it is associated with spin fluctuation scattering. Following this, the transitions at T_{N1} and T_{N2} both reduce $\rho(T)$ due to the removal of spin disorder scattering. $\rho(T)$ finally saturates towards a value near $1.5 \mu\Omega \text{ cm}$ at low temperatures, showing that there is little disorder due to crystalline defects. The influence of a magnetic field applied for $H \parallel$ and $\perp c$ are shown in Figs. 4(a) and 4(b). Although the overall value of $\rho(T)$ is enhanced with increasing field, the ordering temperatures remain nearly constant.

Figs. 4(d) and 4(e) show the magnetoresistance $\rho(H)$ for electrical current I applied in the ab -plane with $H \parallel$ and \perp to the c -axis. At the lowest temperatures, $\rho(H)$ is roughly linear over a wide range of fields for $H \parallel c$, with no evidence for metamagnetic phase transitions. $\rho(H)$ subsequently develops weak positive curvature as the temperature is raised through T_{N1} and T_{N2} . As noted previously for $\text{GdAuAl}_4\text{Ge}_2$ and $\text{TbAuAl}_4\text{Ge}_2$ ($I \parallel ab$, $H \parallel c$), this differs from the conventional quadratic magnetoresistance associated with orbital charge carriers' motion and suggests the presence of an unconventional scatter-

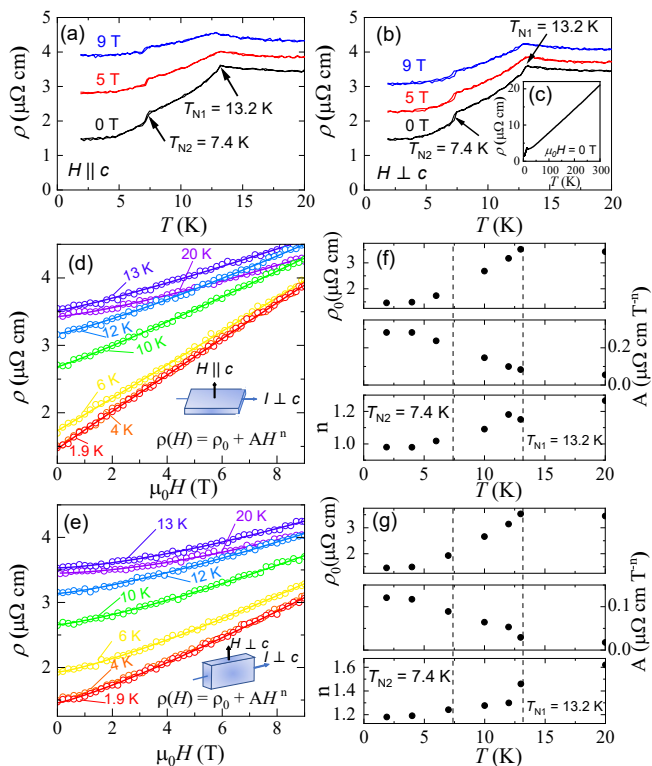


FIG. 4. (a) Electrical resistivity $\rho(T)$ of $\text{SmAuAl}_4\text{Ge}_2$ near T_{N1} and T_{N2} shown at different applied fields along the c -axis and (b) perpendicular to the c -axis. Data were collected both for zero field cooling and field cooling. (c) $\rho(T)$ for $1.8 < T < 300$ K. (d) Isothermal magnetoresistance $\rho(H)$ at different temperatures for magnetic field applied along c -axis ($H \parallel c$) and (e) perpendicular to the c -axis ($H \perp c$). The electrical current remains in the ab -plane for both cases. The insets show the schematics of the measurement configurations respectively. The data points are represented by open circles and the fits are shown as solid lines. (f) and (g) The temperature dependence of the parameters ρ_0 , A , and n resulting from fits to the data in (d) and (e), respectively. The dotted vertical lines represent the locations of the ordering temperatures T_{N1} and T_{N2} .

ing process [30]. In contrast, $\rho(H)$ for $H \perp c$ exhibits positive curvature even at low temperatures, again without evidence for any metamagnetic phase transition. To quantify these behaviors, we carried out fits to the data using a power law expression $\rho(H) = \rho_0 + AH^n$, which accounts for the residual resistivity ρ_0 and the field dependence that arises from the combined electronic and magnetic scattering behaviors. For $H \parallel c$, as shown in Fig. 4 (f), n gradually increases from 1 to 1.3, indicating the persistence of a single dominant scattering mechanism. For $H \perp c$, as shown in Fig. 4 (g), n initially gradually rises from a value near 1.2 until it abruptly increases near T_{N1} , presumably as a result of a change changes in the magnetic scattering.

	χ_0 (cm ³ /mol)	θ (K)	μ_{eff}/μ_B	C_0 (emuK/mol)	ν
χ_{\perp}	9.50×10^{-4}	-16.3	0.62	3.06×10^{-2}	0.73
χ_{\parallel}	7.05×10^{-4}	-13.8	0.35	3.06×10^{-2}	0.41

TABLE II. Summary of values obtained from fits to the magnetic susceptibility $\chi(T)$ data using Eqn. 2.

IV. DISCUSSION

These data reveal that $\text{SmAuAl}_4\text{Ge}_2$ exhibits complex magnetic ordering that emerges from a non-Curie-Weiss paramagnetic state. In order to understand this, we first consider a minimal model for the paramagnetism which assumes both that the trivalent f -electron state ($4f^5$) dominates the magnetic phenomena and that the crystal electric field (CEF) splitting is sized such that it impacts $\chi(T)$ at and below room temperature. As discussed in Ref. [15], the standard Curie Weiss like temperature dependence $\chi(T) = C/(T - \theta)$ is only valid (i) if all of the crystal field split orbitals are homogeneously occupied or (ii) if $T \ll \Delta_0/k_B$ and the quadratic H dependence in the Zeeman splitting is negligible [15]. Condition ii is unique to 4 f electron systems, where the scale of Δ_0 (the lowest crystal electric field splitting energy) is significantly lower than that of 3 d counterparts. In this situation, the magnetic susceptibility is given by the expression,

$$\chi(T) = \chi_0 + \frac{\nu C_0}{T - \nu\theta} \quad (2)$$

where C_0 is the Curie constant ($C_0 = \frac{N_A \mu_0 \mu_B^2 g_J^2}{k_B}$), θ is the Curie-Weiss temperature, and $\nu = g/g_J$ is a scaled Landé g -factor ($g_J = \frac{2}{7}$). Fits to $\chi(T)$ using Eq. (2) are shown in Fig. 5 and the resulting parameters are summarized in Table II. Importantly, the fits are only expected to work before the first excited state begins to be populated, which is evidenced in the data by the broad maximum that appears in $(\chi_{\parallel} - \chi_0)^{-1}$ near 200 K. Based on this, the lower bound of Δ_0 can be estimated to be on the order of few tens of meV (a few hundreds of Kelvin) [15]. Using the g -factor found from the fit, the effective moment $\mu_{\text{eff}} = g \mu_B \sqrt{J(J+1)}$ (where total angular momentum $J=5/2$ was used for Sm^{3+}) is found $0.62 \mu_B$ and $0.35 \mu_B$ for $H \parallel$ and \perp to c , respectively. These values are slightly reduced from the full Sm^{3+} value of $0.85 \mu_B$ [46], and the differing values of μ_{eff} are associated with the anisotropy of the ν values. Finally, the negative Curie-Weiss temperatures indicate the presence of antiferromagnetic spin exchange interactions.

While this picture qualitatively describes the data, there also are several features that deviate from it. First, we note that $1/\chi_{\perp}(T)$ is strongly suppressed from the fit values below 70 K. The reason for this is not clear, but we speculate that it might be attributed to anisotropic spin fluctuations in the vicinity of ordering temperature: e.g., relating to spin frustration in the ab plane. It is also important to note that different minima in $\chi(T)$ are

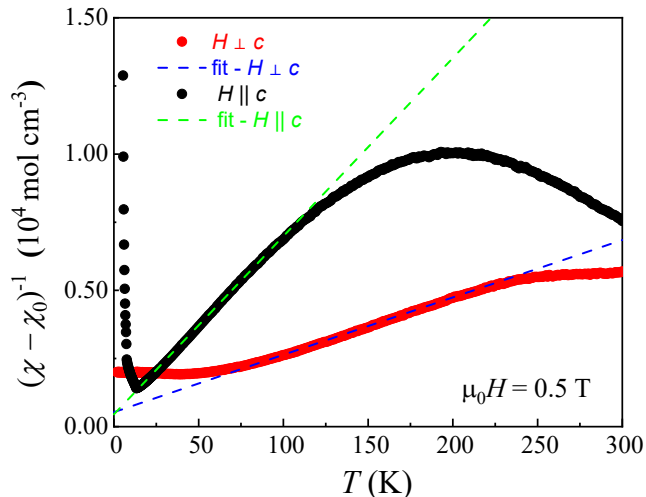


FIG. 5. Inverse magnetic susceptibilities $(\chi - \chi_0)^{-1}$ for $\text{SmAuAl}_4\text{Ge}_2$ and the fitting results of Eq. (2) (dashed line) are shown for both $H \perp c$ and $H \parallel c$ configuration.

observed for the two field directions. This is unexpected since CEF splitting in zero field is isotropic, and thus should impact both curves in similar ways. This implies that additional effects (e.g., van Vleck splitting between the $J = 5/2$ and $7/2$ states) may need to be considered to fully understand this unusual paramagnetic state. A spectroscopy study such as inelastic neutron scattering will be useful to render an accurate CEF characterization.

This behavior contrasts with what is seen for other $\text{LnAuAl}_4\text{Ge}_2$ analogues with conventional Curie-Weiss paramagnetism (Table III), and might lead to the expectation that the ground state would show distinct behavior. Despite this, there are noteworthy similarities in the ordered states between $\text{SmAuAl}_4\text{Ge}_2$ and its analogs. This is highlighted in Fig. 6, where we plot the ordering temperatures for several examples ($\text{Ln} = \text{Ce}, \text{Nd}, \text{Sm}, \text{Gd}, \text{Tb}, \text{and Dy}$) and the de Gennes scaling factor ($G = (g_J - 1)^2 J(J + 1)$) vs. lanthanide [48, 49]. From this, it is clear that there is close agreement between G and the trends seen in the ordering temperatures, indicating that these compounds have a shared spin exchange mechanism. An explanation for this could be that while each of these compounds has a different CEF splitting for the f -electron state, which impacts the effective magnetic moment, they all share similar Fermi surface topographies. This would result in them having similar conduction electron-mediated RKKY spin interactions that are robust against variations of the lanthanide ion. Indeed, this is expected in the absence of hybridization between the f - and conduction electron.

Another important distinction between $\text{SmAuAl}_4\text{Ge}_2$ and its relatives is the lack of metamagnetic phase transitions. This is puzzling, but given that the $M(H)$ curves for $\text{SmAuAl}_4\text{Ge}_2$ are non-saturating at 7 T, one possibility is that they will appear at larger fields than those

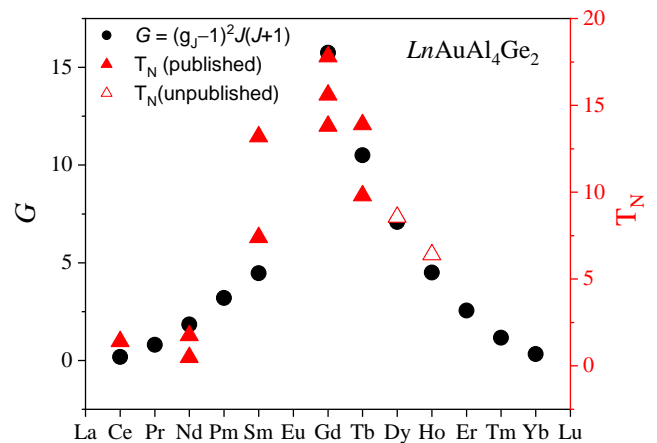


FIG. 6. Comparison between the de Gennes scaling factor G (defined in the text) and the ordering temperatures T_{N1} and T_{N2} (triangles) for the $\text{LnAuAl}_4\text{Ge}_2$ series. Data for $\text{Ln} = \text{Ce}, \text{Nd}, \text{Gd}, \text{and Tb}$ are from Refs. [28–31]. Empty triangles are from unpublished data [47].

accessed in this study. The reason for this might be that the relatively small Sm magnetic moment modifies the internal field in a way that enhances the field-driven transition energy scale. Alternatively, it is possible that both measured directions represent hard magnetic axes. More detailed measurements (e.g., exploring the in-plane magnetic anisotropy) will be useful to address this question.

It is also appealing to consider that the RKKY interaction alone may not fully account for the complex magnetic order. All of these compounds, with the exception of $\text{CeAuAl}_4\text{Ge}_2$, exhibit multiple temperature and field-dependent transitions, indicating the presence of magnetic frustration. This motivates the need for further work to understand effects arising from (i) competing RKKY interactions: e.g., as seen for the anisotropic next nearest neighbor Ising model[50] and (ii) geometric frustration. In any case, these behaviors open an intriguing path for stabilizing and tuning nontrivial spin states: e.g., similar to what is seen for the structurally similar Gd_2PdSi_3 [23], where a unique combination of spin anisotropy with a centrosymmetric triangular Gd lattice produces an unusual skyrmion state. For the $\text{LnAuAl}_4\text{Ge}_2$ compounds, if skyrmions or other nontrivial magnetic textures do not appear in the $T - H$ phase diagram of one of the parent compounds, it may be possible to access them by chemically mixing the f -element site. This would preserve the structural constraints but vary the magnetic anisotropy, magnetic moment, and the resulting $T - H$ phase diagrams.

Finally, it is intriguing that linear magnetoresistance is seen for fields applied along c -axis. This is similar to what is seen for the Gd and Tb analogues [30], and based on this commonality we infer that the underlying origin for this behavior is independent of the details of the f -electron state. This naturally leads us to consider that it connects to electronic degrees of freedom that are

	Ce[28]	Nd[31]	Sm	Gd[29]	Tb[29]
T_{N1} (K) - ZFC	1.40	1.75	13.2	17.8	13.9
T_{N2} (K) - ZFC	-	0.49	7.4	15.6	9.8
T_{N3} (K) - ZFC	-	-	-	13.8	-
Anisotropy $\chi_{\parallel}/\chi_{\perp}$ at 1.8K	0.3	1.62	2.53	1.56	5.9
H_{C1} (T)	-	0.04($H \parallel c$)	-	1.9($H \perp c$)	1.3($H \perp c$)
H_{C2} (T)	-	0.75($H \parallel c$)	-	-	1.9($H \perp c$)
H_{C3} (T)	-	1.6 ($H \parallel c$)	-	-	2.7($H \perp c$)
M_{\perp} (μ_B)	1.3	1.23	1.74×10^{-2}	4.9	8.31
M_{\parallel} (μ_B)	0.4	1.41	6.7×10^{-3}	3.65	1.33
$S_{mag}(T = T_{N1})$ (J/(mol-K))	3.00	3.46	4.28	12.8	13.9
$S_{mag}(T = 70K)$ (J/(mol-K))	-	14	0.56	16.4	20.7
$R \ln(2J + 1)$ (J/(mol-K))	14.9	19.1	14.9	17.3	21.3

TABLE III. Summary of magnetic properties for $LnAuAl_4Ge_2$ ($Ln =$ lanthanide) obtained from the magnetic susceptibility $\chi(T)$, magnetization $M(H)$, and heat capacity $C(T)$, where $\chi(T)$ was collected at $\mu_0 H = 0.5$ T and M values here are reported at 7 T and 1.8 K. Magnetic entropy $S_{mag}(T)$ are calculated from $C_{mag}(T)$ (See text). T_{N1} , T_{N2} , and T_{N3} refers the zero field ordering temperatures identified from $\chi(T)$. \perp (\parallel) refers to $H \perp c$ ($H \parallel c$). R refers the gas constant and J is the total angular momentum for each Ln^{3+} ions. Data for $Ln =$ Ce, Nd, Gd, and Tb are from Refs [28–31].

shared amongst all of the chemical analogues. As we noted previously, a possible scenario is that the formation of charge or spin density waves leads to modification of high curvature Fermi surfaces due to zone-folding energy gaps - thereby producing linear magnetoresistance [51–53]. More recently, angle-resolved photoemission spectroscopy measurements also revealed the presence of non-trivial topologically protected bands [54], whose impact on the electrical transport remains to be clarified. In order to investigate these points, it will be of interest to measure the magnetoresistance of the Y, Ce, and Nd analogs, to search for Fermi surface similarities or instabilities (e.g., by detecting quantum oscillations), and to perform measurements to even higher fields to reveal the extent of linear magnetoresistance throughout the entire family.

V. CONCLUSIONS

In summary, we have shown that $SmAuAl_4Ge_2$ exhibits weak paramagnetism that strongly deviates from conventional Curie-Weiss behavior. This is described in terms of crystal electric field splitting, where the energy difference between the ground state and the first excited state is on the order of several tens of meV. Similar to other $LnAuAl_4Ge_2$ analogues, complex antiferromagnetic ordering emerges at low temperatures ($T_{N1} = 13.2$ K and $T_{N2} = 7.4$ K). This behavior likely relates to the geometrically frustrated triangular arrangement of Ln ions in the ab plane, but other factors such as complexity in the RKKY interaction may play an impor-

tant role. The temperature-dependent electrical resistivity and heat capacity indicate standard metallic behavior, although linear magnetoresistance appears within the ordered states over a wide field range. Taken together, this low temperature behavior resembles what is seen for other $LnAuAl_4Ge_2$ materials, with some noteworthy differences including the lack of metamagnetic phase transitions. Thus, $SmAuAl_4Ge_2$ emerges as an environment for complex quantum spin states and unusual magnetotransport behaviors and invites further investigations of the entire family of materials. In particular, it will be useful to measure the order parameters (e.g., using neutron scattering), to quantify the in-plane magnetic anisotropy, to search for metamagnetic phase transitions at even larger magnetic fields, and to develop a better understanding of the Fermi surface topography and possible topology (e.g., using quantum oscillations or angle-resolved photoemission spectroscopy measurements.)

VI. ACKNOWLEDGEMENTS

RB, KF, and OO were supported by the National Science Foundation through NSF DMR-1904361. CB was supported by the National High Magnetic Field Laboratory Research Experience for Undergraduates program. M.L. was supported by the U.S. Department of Energy, Basic Energy Sciences, Materials Sciences and Engineering Division under Award No. DE-SC0021377. The National High Magnetic Field Laboratory is supported by the National Science Foundation through NSF DMR-1644779 and the State of Florida.

- [1] A. P. Ramirez, Strongly Geometrically Frustrated Magnets, *Annual Review of Materials Science* **24**, 453-480 (1994).
- [2] A. P. Ramirez, A. Hayashi, R. J. Cava, R. Siddharthan, and B. S. Shastry, Zero-point entropy in 'spin ice', *Nature* **399**, 333-335 (1999).
- [3] Leon Balents, Spin Liquids in Frustrated Magnets, *Nature* **464**, 199-208 (2010).
- [4] Yi Zhou, Kazushi Kanoda, and Tai-Kai Ng, Quantum spin liquid states, *Reviews of Modern Physics* **89**, 025003 (2017).
- [5] P. W. Anderson, Resonating valence bonds: a new kind of insulator? *Materials Research Bulletin* **8**, 153-160 (1973).
- [6] B. Bernu, C. Lhuillier, and L. Pierre, Signature of Néel order in exact spectra of quantum antiferromagnets on finite lattices, *Phys. Rev. Lett.* **69**, 2590-2593 (1992).
- [7] Ojiro Nagai, Seiji Miyashita, and Tsuyoshi Horiguchi, Ground state of the antiferromagnetic Ising model of general spin S on a triangular lattice, *Phys. Rev. B* **47**, 202-205 (1993).
- [8] Fa Wang and Ashvin Vishwanath, Spin-liquid states on the triangular and Kagomé lattices: A projective-symmetry-group analysis of Schwinger boson states, *Phys. Rev. B* **74**, 174423 (2006).
- [9] Masafumi Tamura and Reizo Kato, Magnetic susceptibility of $\beta' - [\text{Pd}(\text{dmit})_2]$ salts ($(\text{dmit}) = 1, 3 - \text{dithiol} - 2 - \text{thione} - 4, 5 - \text{dithiolate}, \text{C}_3\text{S}_5$): evidence for frustration in spin-1/2 Heisenberg antiferromagnets on a triangular lattice, *Journal of Physics: Condensed Matter* **14**, L729 (2002).
- [10] K. W. Plumb, J. P. Clancy, L. J. Sandilands, V. Vijay Shankar, Y. F. Hu, K. S. Burch, Hae-Young Kee, and Young-June Kim, $\alpha - \text{RuCl}_3$: A spin-orbit assisted Mott insulator on a honeycomb lattice, *Phys. Rev. B* **90**, 041112 (2014).
- [11] A. Banerjee, C. A. Bridges, J.-Q. Yan, A. A. Aczel, L. Li, M. B. Stone, G. E. Granroth, M. D. Lumsden, Y. Yiu, J. Knolle, S. Bhattacharjee, D. L. Kovrizhin, R. Moessner, D. A. Tennant, D. G. Mandrus, and S. E. Nagler, Proximate Kitaev quantum spin liquid behaviour in a honeycomb magnet, *Nature Mater* **15**, 733-740 (2016).
- [12] Michael A. McGuire, Crystal and Magnetic Structures in Layered, Transition Metal Dihalides and Trihalides, *Crystals* **7**, 121 (2017).
- [13] E. D. L. Rienks, S. Wimmer, J. Sánchez-Barriga, O. Caha, P. S. Mandal, J. Růžička, A. Ney, H. Steiner, V. V. Volobuev, H. Groiss, M. Albu, G. Kothleitner, J. Michalička, S. A. Khan, J. Minár, H. Ebert, G. Bauer, F. Freyse, A. Varykhalov, O. Rader, and G. Springholz, Large magnetic gap at the Dirac point in $\text{Bi}_2\text{Te}_3/\text{MnBi}_2\text{Te}_4$ heterostructures, *Nature* **576**, 423-428 (2019).
- [14] Yuesheng Li, Gang Chen, Wei Tong, Li Pi, Juanjuan Liu, Zhaorong Yang, Xiaoqun Wang, and Qingming Zhang, Rare-Earth Triangular Lattice Spin Liquid: A Single-Crystal Study of YbMgGaO_4 , *Phys. Rev. Lett.* **115**, 167203 (2015).
- [15] Christopher A. Pocs, Peter E. Siegfried, Jie Xing, Athena S. Sefat, Michael Hermele, B. Normand, and Minhyea Lee, Systematic extraction of crystal electric-field effects and quantum magnetic model parameters in triangular rare-earth magnets, *Phys. Rev. Res.* **3**, 043202 (2021).
- [16] M. A. Ruderman and C. Kittel, Indirect Exchange Coupling of Nuclear Magnetic Moments by Conduction Electrons, *Phys. Rev.* **96**, 99-102 (1954).
- [17] Kei Yosida, Magnetic Properties of Cu-Mn Alloys, *Phys. Rev.* **106**, 893-898 (1957).
- [18] Tadao Kasuya, A Theory of Metallic Ferro- and Antiferromagnetism on Zener's Model, *Progress of Theoretical Physics* **16**, 45-57 (1956).
- [19] Mingu Kang, Shiang Fang, Linda Ye, Hoi Chun Po, Jonathan Denlinger, Chris Jozwiak, Aaron Bostwick, Eli Rotenberg, Efthimios Kaxiras, Joseph G. Checkelsky, and Riccardo Comin, Topological flat bands in frustrated kagome lattice CoSn , *Nature Communications* **11**, 4004 (2020).
- [20] B. C. Sales, W. R. Meier, A. F. May, J. Xing, J.-Q. Yan, S. Gao, Y. H. Liu, M. B. Stone, A. D. Christianson, Q. Zhang, and M. A. McGuire, Tuning the flat bands of the kagome metal CoSn with Fe, In, or Ni doping, *Physical Review Materials* **5**, 044202 (2021).
- [21] R. Brenden, L. C. Ortiz, J. R. Gomes, M. W. Morey, M. Bordelon, J. S. Mangum, I. W. H. Oswald, J. A. Rodriguez-Rivera, J. R. Neilson, S. D. Wilson, E. Ertekin, T. M. McQueen, and E. S. Toberer, New kagome prototype materials: discovery of KV_3Sb_5 , RbV_3Sb_5 , and CsV_3Sb_5 , *Physical Review M* **3**, 094407 (2019).
- [22] Brenden R. Ortiz, Samuel M.L. Teicher, Yong Hu, Julia L. Zuo, Paul M. Sarte, Emily C. Schueller, A.M. Milinda Abeykoon, Matthew J. Krogstad, Stephan Rosenkranz, Raymond Osborn, Ram Seshadri, Leon Balents, Junfeng He, and Stephen D. Wilson, CsV_3Sb_5 : A \mathbb{Z}_2 Topological Kagome Metal with a Superconducting Ground State, *Physical Review Letters* **125**, 247002 (2020).
- [23] Takashi Kurumaji, Taro Nakajima, Max Hirschberger, Akiko Kikkawa, Yuichi Yamasaki, Hajime Sagayama, Hironori Nakao, Yasujiro Taguchi, Taka-hisa Arima, and Yoshinori Tokura, Skyrmion lattice with a giant topological Hall effect in a frustrated triangular-lattice magnet, *Science* **365**, 914 (2019).
- [24] Qi Wang, Shanshan Sun, Xiao Zhang, Fei Pang, and Hechang Lei, Anomalous Hall effect in a ferromagnetic Fe_3Sn_2 single crystal with a geometrically frustrated Fe bilayer kagome lattice, *Physical Review B* **94**, 075135 (2016).
- [25] Qi Wang, Kelly J. Neubauer, Chunruo Duan, Qiangwei Yin, Satoru Fujitsu, Hideo Hosono, Feng Ye, Rui Zhang, Songxue Chi, Kathryn Krycka, Hechang Lei, and Pengcheng Dai, Field-induced topological Hall effect and double-fan spin structure with a c -axis component in the metallic kagome antiferromagnetic compound YMn_6Sn_6 , *Physical Review B* **103**, 014416 (2021).
- [26] Y. Tokiwa, J. J. Ishikawa, S. Nakatsuji, and P. Gegenwart, Quantum criticality in a metallic spin liquid, *Nature Materials* **13**, 356-359 (2014).
- [27] Xiuni Wu and Mercouri G. Kanatzidis, $\text{REAuAl}_4\text{Ge}_2$ and $\text{REAuAl}_4(\text{Au}_x\text{Ge}_{1-x})_2$ ($\text{RE} = \text{rare earth element}$): Quaternary intermetallics grown in liquid aluminum, *Journal of Solid State Chemistry* **178**, 3233-3242 (2005).
- [28] S. Zhang, N. Aryal, K. Huang, K. W. Chen, Y. Lai, D. Graf, T. Besara, T. Siegrist, E. Manousakis, and R. E. Baumbach, Electronic structure and magnetism in the

- layered triangular lattice compound $\text{CeAuAl}_4\text{Ge}_2$, *Physical Review Materials* **1**, 044404 (2017).
- [29] Keke Feng, Ian Andreas Leahy, Olatunde Oladehin, Kaya Wei, Minhyea Lee, and Ryan Baumbach, Magnetic ordering in $\text{GdAuAl}_4\text{Ge}_2$ and $\text{TbAuAl}_4\text{Ge}_2$: Layered compounds with triangular lanthanide nets, *Journal of Magnetism and Magnetic Materials* **564**, 170006 (2022).
- [30] Ian A. Leahy, Keke Feng, Roei Dery, Ryan Baumbach, and Minhyea Lee, Field-induced magnetic states in the metallic rare-earth layered triangular antiferromagnet $\text{TbAuAl}_4\text{Ge}_2$, *Physical Review B* **106**, 094426 (2022).
- [31] Mengru Cong, Han Ge, Lei Zhang, Weijun Ren, Nan Zhao, Tiantian Li, Shanmin Wang, Jinlong Zhu, Jiawei Mei, Qiang Zhang, Jieming Sheng, Fei Gao, Bing Li, Zhidong Zhang, and Liusuo Wu, Magnetic phase diagram and multiple field-induced states in the intermetallic triangular-lattice antiferromagnet $\text{NdAuAl}_4\text{Ge}_2$ with Ising-like spins, *Physical Review Materials* **7**, 024423 (2023).
- [32] S. Shin, V. Pomjakushin, L. Keller, P. F. S. Rosa, U. Stuhr, C. Niedermayer, R. Sibille, S. Toth, J. Kim, H. Jang, S.-K. Son, H.-O. Lee, T. Shang, M. Medarde, E. D. Bauer, M. Kenzelmann, and T. Park, Magnetic structure and crystalline electric field effects in the triangular antiferromagnet $\text{CePtAl}_4\text{Ge}_2$, *Physical Review B* **101**, 224421 (2020).
- [33] J. H. van Vleck, *The Theory of Electric and Magnetic Susceptibilities*, Oxford, Oxford University Press, 245-256 (1965).
- [34] Surjeet Singh, Surajit Saha, S. K. Dhar, R. Suryanarayanan, A. K. Sood, and A. Revcolevschi, Manifestation of geometric frustration on magnetic and thermodynamic properties of the pyrochlores $\text{Sm}_2\text{X}_2\text{O}_7$ ($X = \text{Ti, Zr}$), *Physical Review B* **77**, 054408 (2008).
- [35] Shotaro Sanada, Yuji Aoki, Hidekazu Aoki, Akihisa Tsuchiya, Daisuke Kikuchi, Hitoshi Sugawara, and Hideyuki Sato, Exotic heavy-fermion state in filled skutterudite $\text{SmOs}_4\text{Sb}_{12}$, *Journal of the Physical Society of Japan* **74**, 246-249 (2005).
- [36] W. M. Yuhasz, N. A. Frederick, P. C. Ho, N. P. Butch, B. J. Taylor, T. A. Sayles, M. B. Maple, J. B. Betts, A. H. Lacerda, P. Rogl, and G. Giester, Heavy-fermion behavior, crystalline electric field effects, and weak ferromagnetism in $\text{SmOs}_4\text{Sb}_{12}$, *Physical Review B* **71**, 104402 (2005).
- [37] R. Gumenuik, M. Schöneich, A. Leithe-Jasper, W. Schnelle, M. Nicklas, H. Rosner, A. Ormeci, U. Burkhardt, M. Schmidt, U. Schwarz, M. Ruck and Yu Grin, High-pressure synthesis and exotic heavy-fermion behaviour of the filled skutterudite $\text{SmPt}_4\text{Ge}_{12}$, *New Journal of Physics* **12**, 103035 (2010).
- [38] Ryuji Higashinaka, Takuya Maruyama, Akihiro Nakama, Ryoichi Miyazaki, Yuji Aoki, and Hideyuki Sato, Unusual field-insensitive phase transition and Kondo behavior in $\text{SmTi}_2\text{Al}_{20}$, *Journal of the Physical Society of Japan* **80**, 093703 (2011).
- [39] A. Menth, E. Buehler, and T. H. Geballe, Magnetic and Semiconducting Properties of SmB_6 , *Physical Review Letters* **22**, 295 (1969).
- [40] Maxim Dzero, Kai Sun, Victor Galitski, and Piers Coleman, Topological Kondo Insulators, *Physical Review Letters* **104**, 106408 (2010).
- [41] H.C. Hamaker, L.D. Woolf, H.B. MacKay, Z. Fisk, and M.B. Maple, Coexistence of superconductivity and antiferromagnetic order in SmRh_4B_4 , *Solid State Communications* **32**, 289-294 (1979).
- [42] A. Jayaraman, V. Narayanamurti, E. Bucher, and R. G. Maines, Continuous and Discontinuous Semiconductor-Metal Transition in Samarium Monochalcogenides Under Pressure, *Physical Review Letters* **25**, 1430 (1970).
- [43] K. Momma and F. Izumi, VESTA 3 for three-dimensional visualization of crystal, volumetric and morphology data, *J. Appl. Crystallogr.*, **44**, 1272-1276 (2011).
- [44] M. Bouvier, P. Lethuillier, and D. Schmitt, Specific heat in some gadolinium compounds. I. Experimental, *Physical Review B* **43**, 13137 (1991).
- [45] *Physical Property Measurement System Heat Capacity Option User's Manual*, Chapter 4.3.4, Slope Analysis of Relaxation Curves, and Chapter 4.6.2, Slope Analysis, 19th edition, Quantum Design, San Diego, CA, (2010)
- [46] Stephen Blundell, *Magnetism in Condensed Matter*, ch. 2, Isolated magnetic moments, Oxford University Press, p.34 (2001).
- [47] Keke Feng and Ryan Baumbach, unpublished data.
- [48] P.G. De Gennes, Interactions indirectes entre couches 4f dans les métaux de terres rares, *J. Phys. Radium* **23**, 510-521 (1962).
- [49] W. C. Koehler, Magnetic properties of rare-earth metals and alloys, *Journal of Applied Physics* **36**, 1078-1087 (1965).
- [50] Walter Selke, The ANNNI model-Theoretical analysis and experimental application, *Physics Reports* **170**, 213-264 (1988).
- [51] Kamil K. Kolincio, Marta Roman, and Tomasz Klimczuk, Enhanced Mobility and Large Linear Nonsaturating Magnetoresistance in the Magnetically Ordered States of TmNiC_2 , *Physical Review Letters* **125**, 176601 (2020).
- [52] S. Tsuda, C. L. Yang, Y. Shimura, K. Umeo, H. Fukuoka, Y. Yamane, T. Onimaru, T. Takabatake, N. Kikugawa, T. Terashima, H. T. Hirose, S. Uji, S. Kittaka, and T. Sakakibara, Metamagnetic crossover in the quasikagome Ising Kondo-lattice compound CeIrSn , *Physical Review B* **98**, 155147 (2018).
- [53] Yejun Feng, Yishu Wang, D.M. Silevitch, J.-Q. Yan, Riki Kobayashi, Masato Hedod, Takao Nakamad, Yoshichika Onuki, A.V. Suslove, B. Mihaila, P.B. Littlewood, and T. F. Rosenbaum, Linear magnetoresistance in the low-field limit in density-wave materials, *Proceedings of the National Academy of Sciences* **116**, 11201-11206 (2019).
- [54] Chengcheng Zhang, Yuan Wang, Fayuan Zhang, Hongtao Rong, Yongqing Cai, Le Wang, Xiao-Ming Ma, Shu Guo, Zhongjia Chen, Yanan Wang, Zhicheng Jiang, Yichen Yang, Zhengtai Liu, Mao Ye, Junhao Lin, Jiawei Mei, Zhanyang Hao, Zijuan Xie, and Chaoyu Chen, Multiple surface states, nontrivial band topology and antiferromagnetism in $\text{GdAuAl}_4\text{Ge}_2$, *Chinese Physics B* (2023).